



HAL
open science

Heterodyne holographic microscopy of gold particles

Michael Atlan, Michel Gross, Pierre Desbiolles, Emilie Absil, Gilles Tessier,
Maité Coppey-Moisan

► **To cite this version:**

Michael Atlan, Michel Gross, Pierre Desbiolles, Emilie Absil, Gilles Tessier, et al.. Heterodyne holographic microscopy of gold particles. 2007. hal-00194121v1

HAL Id: hal-00194121

<https://hal.science/hal-00194121v1>

Preprint submitted on 10 Dec 2007 (v1), last revised 21 Feb 2008 (v2)

HAL is a multi-disciplinary open access archive for the deposit and dissemination of scientific research documents, whether they are published or not. The documents may come from teaching and research institutions in France or abroad, or from public or private research centers.

L'archive ouverte pluridisciplinaire **HAL**, est destinée au dépôt et à la diffusion de documents scientifiques de niveau recherche, publiés ou non, émanant des établissements d'enseignement et de recherche français ou étrangers, des laboratoires publics ou privés.

Heterodyne holographic microscopy of gold particles.

Michael Atlan,^{1,*} Michel Gross,¹ Pierre Desbiolles,¹ Émilie Absil,² Gilles Tessier,² and Maité Coppey-Moisan³

¹Laboratoire Kastler-Brossel de l'École Normale Supérieure, CNRS UMR 8552, Université Pierre et Marie Curie - Paris 6, 24 rue Lhomond 75231 Paris cedex 05. France

²École Supérieure de Physique et de Chimie Industrielles de la Ville de Paris, CNRS UPR 5, Université Pierre et Marie Curie - Paris 6, 10 rue Vauquelin 75231 Paris cedex 05. France

³Département de Biologie Cellulaire, Institut Jacques Monod, CNRS UMR 7592, Université Paris 6 and 7, 2 Place Jussieu, Tour 43, 75251 Paris Cedex 05. France

(Dated: December 10, 2007)

We report experimental results on heterodyne holographic microscopy of subwavelength-sized gold particles. The apparatus uses continuous green laser illumination of the metal beads in a total internal reflection configuration for dark-field operation. Detection of the scattered light at the illumination wavelength on a charge-coupled device array detector enables 3D localization of brownian particles in water.

OCIS : 180.6900, 090.1995, 170.0180

Assessing microscopic processes by tracking optical labels has a broad range of applications in biology. Fluorescent molecules are widely used in this aim, but the observation time is limited by photobleaching. Quantum dots offer a much better photostability, but they have the inconvenient to blink. Noble metal nanoparticles have the advantage of be perfectly photostable [1]. Originally, light scattered by small noble metal particles has been detected in dark field [1] or total internal reflection [2] configuration. To improve the detection sensitivity, interferometric approaches have been introduced [3, 4, 5, 6, 7]. Common-path interference, originally achieved with a Nomarski interferometer [8], translates phase variations into intensity variations, and enables detection of phase perturbation provoked by spatial [9] or photothermal [10] modulation. Scanning heterodyne detection of the photothermal modulation [3] enables an unmatched combination of sensitivity and selectivity suitable to discriminate particles smaller than 5 nm from their background. Photothermal imaging relies on a spatial scanning of the laser beams to track the index modulation in the neighborhood of the beads; the temporal noise in the incident light leads to spatial noise in the image acquired sequentially [7]. Wide-field detection schemes alleviate such issues, but their sensitivity in optical mixing configurations would not match heterodyne detection on single detectors levels. We propose here a wide-field, shot-noise limited, tunable CCD heterodyne detection technique able to achieve high-resolution, 3D microscopy old particles with a laser source at rates compatible with biological dynamics. The experimental setup is sketched in fig. 1(a).

The main laser beam ($\lambda = 532$ nm, field E_L , 50 mW, single axial mode, CW) is split with a polarizing beam splitter (PBS) cube in local oscillator (LO) and illumination arms (fields E_{LO} and E_I). A $\lambda/2$ waveplate (HWP), and neutral densities (A1, A2) allow control of the optical power in each arm. Both beams are frequency-

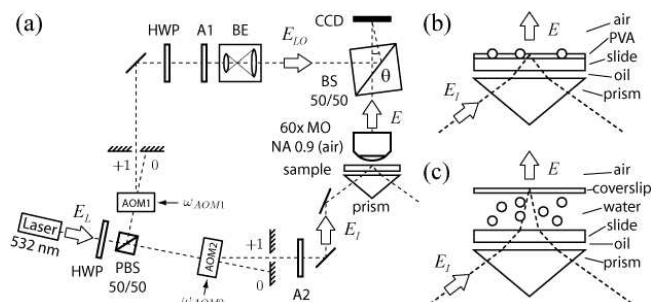


FIG. 1: Experimental setup (a). Evanescent wave illumination of static beads in a plane (b). Total internal reflection configuration for dark-field illumination of beads in a tridimensional environment (c). Acronyms defined in the text.

shifted around 80 MHz by acousto-optic modulators (AOM) driven at frequencies ω_{AOM1} , ω_{AOM2} . The LO beam passes through a beam expander (BE) to form a plane wave whose polarization angle is adjusted with a HWP to maximize the holographic modulation depth. The object is illuminated in dark field configuration by using total internal reflection (TIR). The scattered field $E \ll E_{LO}$ passes through a microscope objective (MO, 60 \times magnification, NA = 0.9, air). Off-axis optical mixing (θ tilt) of E with E_{LO} with a beam splitter (BS) results in an interference pattern recorded with a CCD camera (PCO Pixelfly QE, 1392 \times 1024 square pixels of 6.7 μ m, frame rate $\omega_S = 12$ Hz). Proper frequency detuning $\Delta\omega = \omega_{AOM2} - \omega_{AOM1}$, and angular tilt θ of enables accurate and sensitive phase-shifting off-axis holography [11, 12].

The first samples observed are thin layers of gold beads (diameter $d = 50$ nm to 200 nm) immobilized in a polyvinyl alcohol (PVA) matrix spread by spin coating onto a glass slide. These slides are set onto a prism used to guide the illumination field E_I and provoke TIR at the PVA-air interface. Microscope immersion oil between the

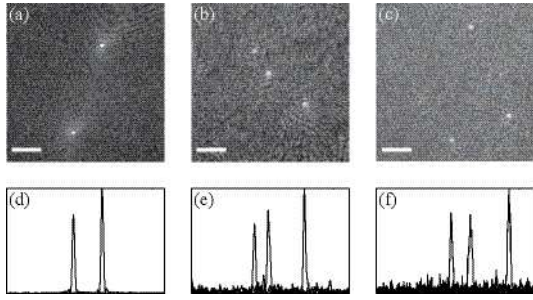


FIG. 2: Squared amplitude holograms $|E|^2$ in logarithmic arbitrary units. 200 nm beads (a), 100 nm beads (b), and 50 nm beads (c). Scale bar is $10 \mu\text{m}$. Horizontal profile traces of $|E|^2$ at the beads positions, averaged over 4 pixels (d, e, f), in linear arbitrary units.

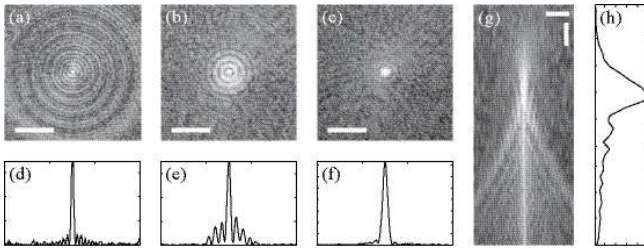


FIG. 3: $|E|^2$ reconstructed images of a 200 nm gold bead with experimental setup of fig.1(b) at several axial positions : $z = 22 \mu\text{m}$ (a) $z = 17 \mu\text{m}$ (b) $z = 0 \mu\text{m}$ (c), displayed in logarithmic arbitrary units. Scale bar is $5 \mu\text{m}$. Transverse plane profile traces of $|E|^2$ at the beads positions, averaged over 3 pixels ((d) to (f)), in linear arbitrary units. Axial plane distribution (g) and linear scale profile averaged over 10 pixels in the lateral direction (h).

prism and the slide enables refractive index matching. The evanescent wave locally frustrated by the beads is turned into a propagative scattered field E collected by the MO. To make E and E_{LO} in phase opposition from one frame to the next, two-phase detection ($\Delta\omega = \omega_S/2$) is performed. Exposure time is $\tau_E = 50 \text{ ms}$, and holograms are obtained by making the difference of consecutive frames. The complex field $E(x, y, z)$, in the beads plane z , is reconstructed by numerical Fresnel transform [11].

Fig.2 shows the bead images (a,b,c), and the corresponding intensity profiles along x (d,e,f). The images are obtained by averaging ($|E(x, y, z)|^2$) over 4 sequences of 2 images. The beads diameters are 200 (a,d), 100 (b,e) and 50 nm (c,f). Under 50 nm the coherent parasitic light due to dust or surface roughness prevents the beads to be perfectly distinguished. Fig.3 shows, for 200 nm beads, the x, y images (a,b,c) and the x profiles (d,e,f), at $z = 0, 17,$ and $22 \mu\text{m}$ relative reconstruction distances. It also shows the x, z image (g) and the z profile (h), in the $z = 0$ to $47 \mu\text{m}$ range. Because the bead emitters are close to a plane dielectric interface [13], one observes an asymmetric signal in the z direction of $\sim 7 \mu\text{m}$ width at

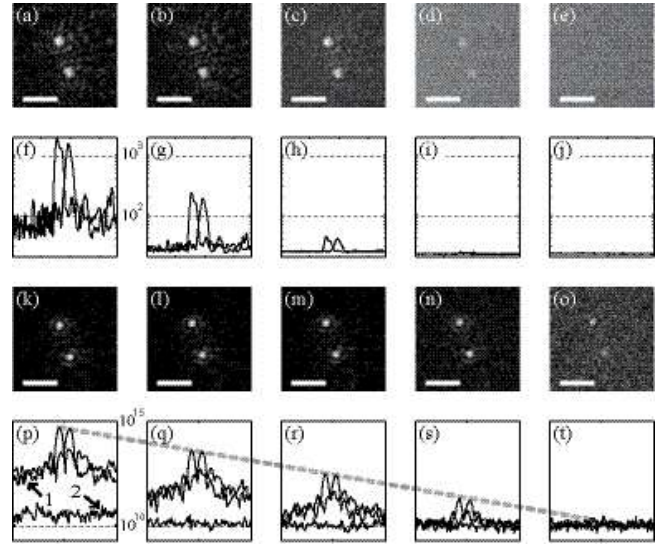


FIG. 4: Intensity images calculated from 4×2 camera frames data of a pair of 200 nm particles. (a) to (e) : direct image (LO beam is off). (k) to (o) : holography (LO beam is on). Scale bar is $5 \mu\text{m}$. Illumination field power attenuation ranges from 10^0 to 10^4 . Bead profiles without (f) to (j), and with LO beam (p) to (t). The vertical axis range (A.U.) is the same for (f) to (j), and (p) to (t).

half maximum with rings in the x, y plane. Similar rings have been observed with quantum dot emitters [14, 15]. Quantitative study of this effect [13, 16], is out of the scope of this letter.

To illustrate the sensitivity of our holographic setup, we have displayed on Fig. 4 images ((a, ..., e) and (k, ..., o)) and profiles ((f, ..., j) and (p, ..., t)) of 200 nm beads at different illumination intensities. The illumination beam ($|E_I|^2$) is attenuated by a factor 10^0 (a,f,k,p), 10^1 (b,g,t,q) ..., 10^4 (c,j,o,t). The LO beam is either off (direct imaging : (a, ..., j)), or on (holographic regime : (k, ..., t)). As seen, the beads are imaged with much better sensitivity with the LO beam, since the bead signal remains visible by reducing the illumination power over 4 orders of magnitude. Moreover, the signal is proportional to illumination (dashed line throughout Fig.4(p) to (t)). We must note that, at high illumination level (p), the bead detection dynamic range is limited by the parasitic light background (arrow 1) which is several orders of magnitude larger than the holographic detection noise floor (arrow 2), which is obtained in a cut from the off-axis quietest region of the reconstructed image, away from the beads region. The noise floor (about 10^{10} A.U.), which is related to shot noise of the LO beam, gives an absolute calibration of the bead peak ($5 \cdot 10^{14}$ A.U. on (k)), since it corresponds to 1 photo electron (e) per pixel [12]. Without attenuation (k), the bead peak, whose area is about 20×20 pixels (see (p)) corresponds thus to $\sim 2 \cdot 10^7 e$. This order of magnitude is expected. One watt of laser yields $\sim 10^{19}$ photons per

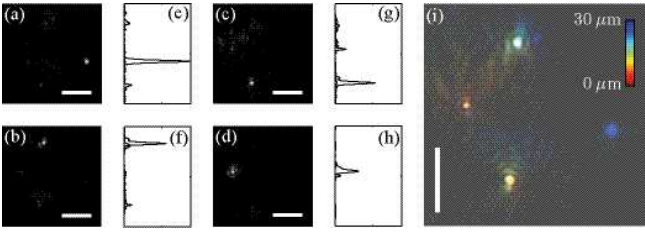


FIG. 5: Axial exploration of a 200 nm gold beads suspension in water. $|E|^2$ images reconstructed $10\ \mu\text{m}$ apart (a) to (d). Linear scale profiles averaged over 4 pixels (e) to (h). Composite image (i). Scale bar is $5\ \mu\text{m}$.

second. With $10\ \text{mW}$ and $2\tau_E = 100\ \text{ms}$ (2 frames to make an hologram), we get 10^{16} photons. The Mie scattering cross section [18] is $0.1\ \mu\text{m}^2$ for $d = 200\ \text{nm}$ and $n = 0.39 - 2.38j$ (gold at $532\ \text{nm}$; $j^2 = -1$). The illumination area is $\sim 1\text{mm}^2$. We get thus 10^9 scattered photons. Since the bead is located at an air glass interface, most of the light (85%) is scattered within the glass [17], and $1.5 \cdot 10^8$ photons are scattered within air within a 2π solid angle. The collection solid angle of a $\text{NA} = 0.9$ objective is $\sim \pi/4$. We then get $4 \cdot 10^7$ photons on the CCD yielding an expected signal of $2 \cdot 10^7$ e (50% quantum efficiency at $532\ \text{nm}$) in agreement with the experiment.

To assess imaging performances in experimental conditions compatible with biological microscopy, we have performed axial sectioning of dynamic beads; we have imaged a suspension of $200\ \text{nm}$ beads in brownian motion in water (see Fig.1(c)). A $\sim 30\ \mu\text{m}$ -thick layer sample is realized within a slide / parafilm (TM) / coverslip stack. The parafilm layer was heated until melting to serve as waterproof spacer of ~ 30 microns thickness. In this configuration, the top interface (coverslip-air) is the one where TIR occurs. The part of the illumination field E_I not diffracted by the beads undergoes TIR while the scattered field E passes through the MO and is used for imaging. Since the exposure time is short : $\tau_E = 1\ \text{ms}$, the LO power is increased to fill the CCD dynamic range. In time τ , brownian particles travel by a distance $r(\tau) = (6D_B\tau)^{1/2}$, where D_B , is the diffusion coefficient ($2.1 \times 10^{-12}\ \text{m}^2 \cdot \text{s}^{-1}$ for water). During one exposure, this travel is smaller than the particle size: $r(1\ \text{ms}) \sim 110\ \text{nm}$. Beads appear thus to be quasi immobile, but because $1/\omega_S = 80\ \text{ms} \gg \tau_E$, beads travel from one image to the next by $r(80\ \text{ms}) \sim 1\ \mu\text{m}$. This property is used for signal demodulation. The hologram is obtained by subtracting from the current recorded frame the time average of the 10 next consecutive frames. By this way the holographic information is recorded in a very short time $\tau_E = 1\ \text{ms}$, and the LO beam component ($|E_{LO}|^2$), which is constant in time, is removed.

Fig.5 shows a series of images (a,b,c,d) and profiles (e,g,f,h) of the sample calculated from a single hologram.

(a) to (d) images and (c) to (h) profiles are calculated for z (a,e) , $z + 10\ \mu\text{m}$ (b,f)... $z + 30\ \mu\text{m}$ (d,h). Image (i) is composed from images (a) to (d), the axial positions being color-coded in composite color distance in the $30\ \mu\text{m}$ range. By performing the reconstruction from a sequence of images, we have obtained the attached multimedia file, which shows the particles in motion, the z position being coded in color.

In this letter we have performed full field imaging of gold nano particules in 3D at video-rate at exposure times as short as $1\ \text{ms}$. Our holographic technique, which benefits from heterodyne gain, exhibits optimal detection sensitivity, and, since the signal can be easily calibrated, we have verified that the signal we get is expected. In future work, low-coherence light sources might be used to reduce the background light component and improve depth-sectioning. Better axial resolution might be obtained by using the phase of the holographic data. The background might also be reduced by a selective modulation (e.g. spatial or photothermal) of the particles.

The authors acknowledge support from French National Research Agency (ANR) and Centre de compétence NanoSciences Île de France (C'nano IdF).

*atlan@lkb.ens.fr

- [1] S. Schultz, D R. Smith, J.J. Mock, and D.A. Schultz. *Proc. Nat. Ac. Sciences*, 97:996, 2000
- [2] C. Sonnichsen, S. Geier, N. E. Hecker et al. *Appl. Phys. Lett.*, 77:2949, 2000
- [3] D. Boyer et P. Tamarat, A. Maali, B. Lounis, and M. Orrit. *Science*, 297:1160, 2002
- [4] K. Lindfors, T. Kalkbrenner, P. Stoller, and V. Sandoghdar. *Phys. Rev. Lett.*, 93:037401, 2004
- [5] M.A. van Dijk M. Lippitz, and M. Orrit. *Phys. Rev. Lett.*, 95:267406, 2005
- [6] F.V. Ignatovich and L. Novotny. *Phys. Rev. Lett.*, 96:013901, 2006
- [7] V. Jacobsen, P. Stoller, C. Brunner, V. Vogel, and V. Sandoghdar. *Optics Express*, 14:405, 2006
- [8] J. S. Batchelder and M. A. Taubenblatt. *Appl. Phys. Lett.*, 55:215, 1989
- [9] J. Hwang and W. E. Moerner. *Opt. Comm.*, 280:487, 2007
- [10] S. Berciaud, D. Lasne, G.A. Blab, L. Cognet, and B.Lounis. *Phys. Rev. B*, 73:045424, 2006
- [11] M. Atlan, M. Gross, and E. Absil. *Opt. Lett.*, 32:1456–1458, 2007.
- [12] M. Gross and M. Atlan. *Opt. Lett.*, 32:909–911, 2007.
- [13] W. Lukosz and R.E. Kunz. *J. Opt. Soc. Am.*, 71:744, 1981.
- [14] M. Speidel A. Jon and E.L. Florin. *Opt. Lett.*, 28:69–71, 2003.
- [15] D. Patra, I. Gregor, J. Enderlein, and M. Sauer. *Appl. Phys. Lett.*, 87:101103, 2005.
- [16] J. Mertz *J. Opt. Soc. Am. B*, 17:1906–1913, 2000.
- [17] X. Brokmann, E. Giacobino, M. Dahan, and JP Hermier. *Appl. Phys. Lett.*, 85:712, 2004.

[18] http://omlc.ogi.edu/calc/mie_calc.html